INVESTIGATION OF IN-SITU ALLOYING GRADE 23 Ti WITH 5at.%Cu BY LASER POWDER BED FUSION FOR BIOMEDICAL APPLICATIONS

E. Newby[1*], I. Yadroitsava [1], P. Krakhmalev [2], D. Kouprianoff[1] and I. Yadroitsev [1]

ABSTRACT

The formation of in-situ grade 23 Ti alloy (Ti6Al4V ELI) with Cu by laser powder bed fusion for application in medical implants was investigated. Ti6Al4V (ELI) powder was mixed with pure Cu powder of similar particle size distribution. Optimal process parameters were investigated for in-situ alloying of Ti6Al4V-5 at.%Cu to form dense parts with suitable microstructural and surface quality. Relations between homogeneity, porosity and process parameters were studied.

[1] Department Mechanical and Mechatronic Engineering, Central University of Technology, Free State, South Africa
[2] Department of Engineering and Physics, Karlstad University, Sweden

1. INTRODUCTION

Infection is one of the common reasons for postoperative complication if a patient received a bone implant. As indicated by Goldfarb *et al.* (2017) in their review, after orthopaedic replacements, the most common complications are: infection, impaired healing, and bleeding affected by surgical and patient risk factors [1]. Bacterial infection of a prosthesis is a severe complication because, in general, the infected prosthesis implant has to be removed in order to cure the infection and a re-implantation operation is needed [2, 3].

Ti6Al4V Extra Low Interstitial (ELI) alloy is commonly used for medical implants because of its biocompatibility and suitable mechanical- and corrosion resistant properties. Manufacturing implants from materials with antibacterial properties such as Cu-bearing alloys is a promising approach to prevent infection [3, 4]. Cu additions at the bone–implant interface reduce the risk of bacterial infection and therefore implant failure [3-5].

The advantage of laser powder bed fusion (LPBF) is that complex shapes can be produced which enables production of custom once-off components, for example bio-medical implants shaped to fit the patient and the exact requirements for bone replacement, but the part quality depends on the manufacturing parameters used. To avoid problems in LPBF; careful selection of process parameters and manufacturing strategies for employed powders by different LPBF systems should be used to avoid porosity from incorrect processing parameters or build conditions, surface roughness and cracks, and reduce high residual stresses and deformation during processing. Due to these challenges, especially for high value and critical parts, such as those for aerospace or medical applications, require process qualification and part quality must be validated. This is discussed in a general review of additive manufacturing (AM) [6] and a review of the use of micro computed tomography for overcoming these issues [7].

The goal of this work was to find optimal process-parameters (based on density and homogeneity of Cu distribution) for LPBF Ti6Al4V-5 at.%Cu in-situ alloyed material for biomedical applications and to study the resulting microstructure.

2. METHODOLOGY AND RESULTS

2.1 Materials and methods

Argon atomized Ti6Al4V (ELI) and Cu powders with spherical particles were used. Chemical composition for Ti6Al4V (ELI) was 89.26 wt% of Ti, 6.31 wt% of Al, 4.09 wt% of V, 0.12% of O, and Cu powder 99.9 % purity (TLS Solutions, LLC). The 10^{th}, 50^{th} and 90^{th} percentiles of equivalent diameter (weighted by volume) were respectively 12.6 μm, 22.9 μm, 37.0 μm for Ti6Al4V (ELI) powder and 9.45 μm, 21.9 μm and 37.5 μm for Cu powder, which means the powder sizes were practically identical. To produce the Ti6Al4V-5 at.% (6.5 wt%) of Cu powder mixture, the elemental Cu and Ti6Al4V(ELI) powders were mixed for 1 hour. Before laser processing, the powder mixture was dried at 80°C for 2 hours without protective atmosphere, to increase powder flowability. To determine optimal laser power and scanning speeds, single tracks with length of 20 mm, single layers and 10 layer samples with size 5 mm x 5 mm were manufactured by an EOSINT M280 machine.

Three tracks were produced at each set of process parameters: 170 W laser power and 0.4–1.4 m/s scanning speeds and 340 W at double the scanning speed accordingly (0.8-2.8 m/s). The powder layer thickness was about 50 μm for single tracks and 30 μm for 3D samples. The building chamber was filled with Ar. Experiments were done on Ti6Al4V substrates with 3 mm thickness.

Single tracks were analysed from top view and then cross-sectioned by wire cutter. Porosity and microstructure of 10-layer samples were studied by optical and scanning electron (SEM) microscopes. SEM was carried out with LEO 1350 FEG operated at 20 kV.

2.2 Results

The morphology of single tracks depends on the laser power and scanning speed. Balling effect started at 1.2-1.4 m/s for 170 W and at 1.6 m/s for 340 W (Fig. 1). Similar results were found by Yadroitsava et al. (2015) for pure Ti6Al4V ELI powder without Cu addition: at 45 μm powder layer, a balling effect started for 170 W laser power at scanning speeds above 1.4 m/s. Further analysis of single tracks showed that at a lower scanning speed of 0.4 m/s more satellites occurred at lateral sides of the tracks (Fig. 2).

For 170 W, the width of the tracks varied from 110 μm at high scanning speeds and shorter interaction time (laser spot diameter divided to the scanning speed), up to 220 μm at 0.4 m/s (Fig. 3a). In terms of linear laser energy density (the ratio of laser power to the scanning speed) no significant difference was found in track width for the similar laser power density (Fig. 3b) which is in accordance with previous results [8]. Analysis of the profile of single tracks shows that at 340 W tracks at scanning speeds V=0.8-1.2 m/s had a smoother surface than the 170 W tracks (Fig. 4).

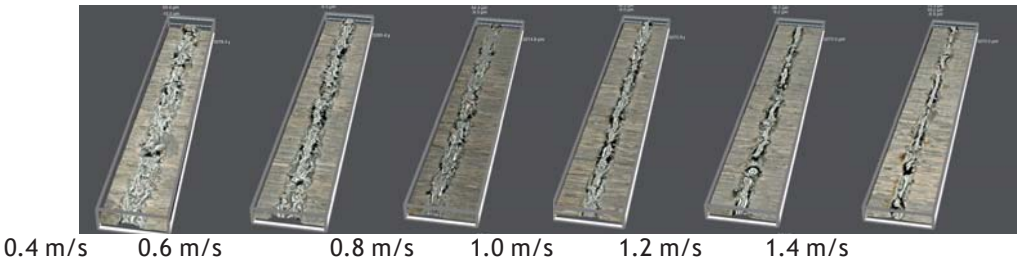

(a)

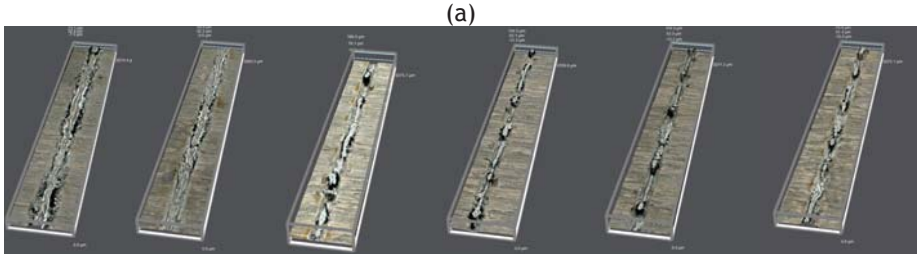

(b)

Fig. 1. 3D reconstruction of single tracks using SmartZoom 5 digital microscope: at 170 W (a) and 340 W. (b).

Fig. 2. Satellites at 170 W laser power and 0.4 m/s scanning speed.

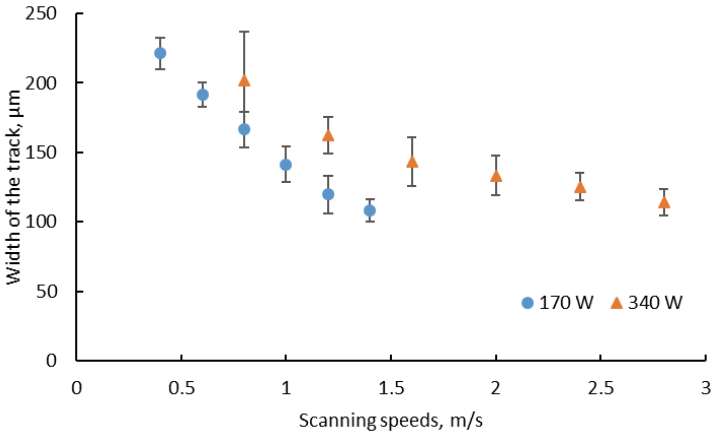

(a)

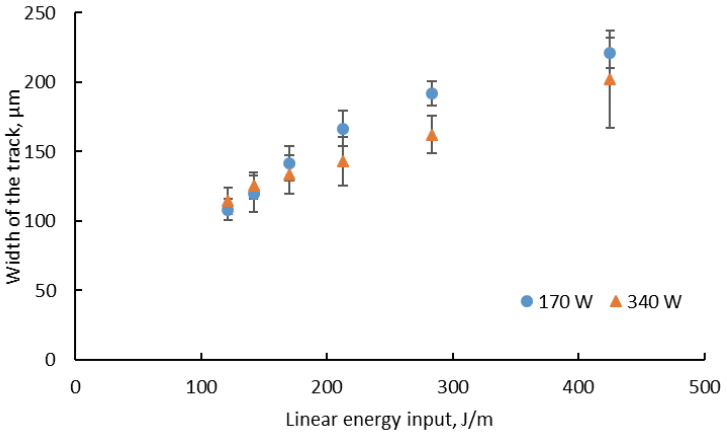

(b)

Fig. 3. Top view measurement of track width *versus* scanning speeds (a) and linear energy input (b).

(a) (b)

Fig. 4. Profiles of tracks at 170 W (a) and 340 W (b) laser power and 1.2 m/s scanning speed.

Analysis of the cross-sections revealed that keyhole mode of laser melting was at 170 W and 0.4-0.6 m/s and for 340 W laser power at 0.8 m/s (Figs. 5 and 6). High laser power lead to high temperatures and when the absorbed energy was sufficient to cause evaporation of the metal, a vapour cavity enhanced the absorption and the laser beam created very deep (V-shape) molten pool (Fig. 6a, scanning speed 0.4-0.6 m/s and Fig. 6b, scanning speed 0.8 m/s). For all other cases, transition or U-shape molten pool, was found. Conduction mode or semi-cylindrical shape of the molten pool was not found.

As Khairallah et al. [9] described, for LPBF, high temperature gradients below the laser beam creates gradient of surface tension that is highly temperature-dependent. That, in turn, creates Marangoni effects and drives the melt flow from the hot laser spot toward the “cold” areas. The recirculated melt flow cools molten metal and leads to spattering, as liquid metal with low viscosity ejects away from the surface. Liquid forms build-up (or “bow wave”) that leads to spattering. The high vapour surface flux (or “gas plume”) exerts a pressure force that ejects liquid metal. When the liquid metal pool elongates, it thins out and breaks up into small droplets due to surface tension tendency to minimize surface energy. The elongation is in the radial direction to the laser spot and pointing away from the melt pool. Thus, more expressed sparking and balling effects can explain stronger variation of width of the tracks at higher laser power.

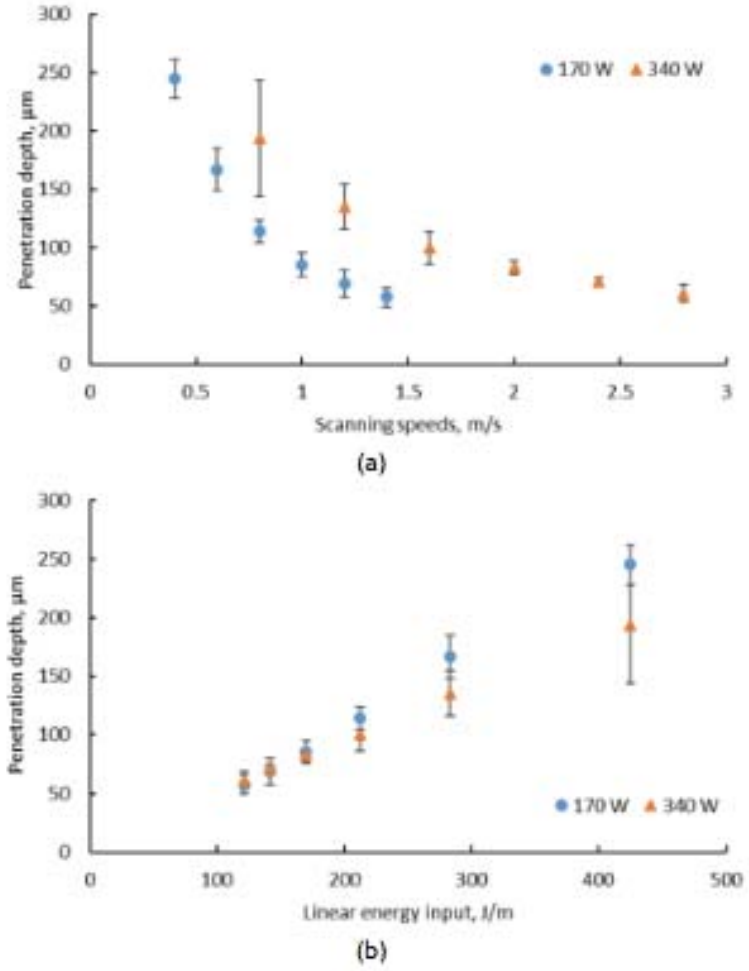

Fig.5. Penetration depth versus scanning speeds (a) and linear energy inputs (b).

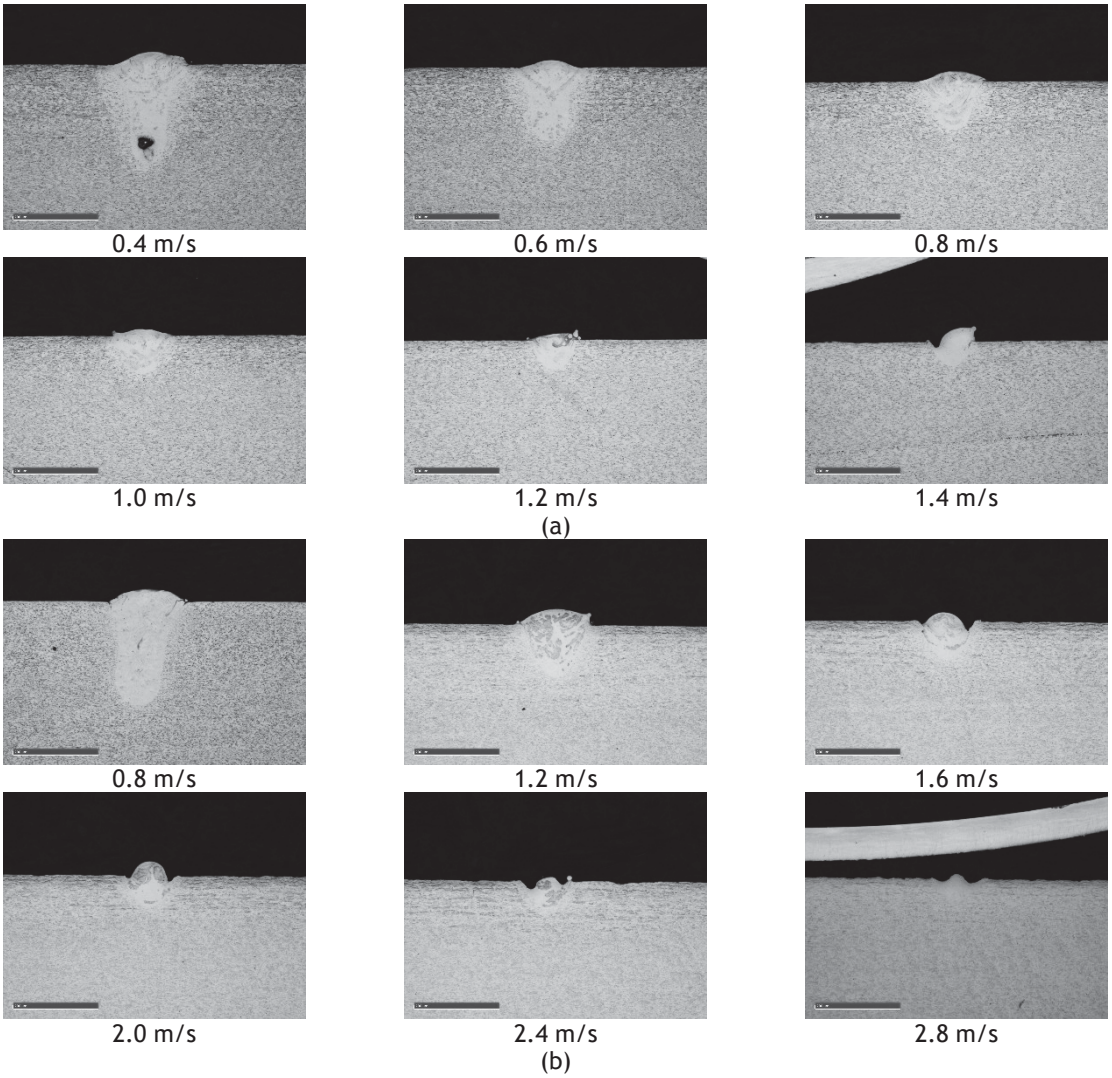

Fig. 6. Cross-sections of single tracks at 170 W (a) and 340 W (b).

By taking the width of the powder tracks into consideration, 80 μm hatch distance was chosen for overlapping for the 3D samples with 10 layers.

Collapse of the created cavity in keyhole mode can leave voids in solidified material. This was clearly seen in cross sectioned analysis of 3D samples (Fig. 7a). It must be noted that big pores were produced in the 170 W samples. At lower laser power the collapse of keyhole happened quicker and created bubbles which did not have enough time to reach the melt pool surface before solidification. Higher laser power led to higher temperature and, respectively, lower viscosity of molten pool which facilitates gas bubbles to escape to the surface of the molten pool. The walls of the capillary are unstable and oscillating in keyhole mode during laser welding and the formation of porosity is very sensitive to the shape of the molten pool at the laser end time [11]. In LPBF, similar phenomena were found [12]. Since small perturbations in the process can cause porosity from LPBF samples during keyhole mode, process-parameters such as 0.4–0.6 m/s, 170 W and 0.8 m/s at 340 W with a powder layer thickness about 50 μm can't be considered as optimal process-parameters for this in-situ alloyed material.

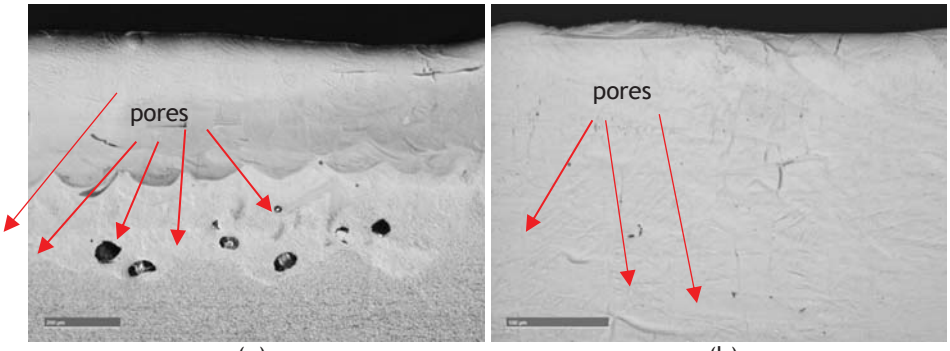

(a) (b)

Fig. 7. Cross-sections of 10 layer samples at 170 W, 0.4 m/s (a) and 340 W at 0.8 m/s (b), keyhole mode.

As it has been shown earlier [13, 14], balling effect provoked porosity in 3D samples. Big pores were found in 3D samples processed at 170 W and 1.4 m/s. Unfused powder particles are clearly visible from the cross-section (Fig. 8a). Interlayer pores were also found at 340 W laser power when scanning speeds were above 1.6 m/s and balling effect occurred (Fig. 8b).

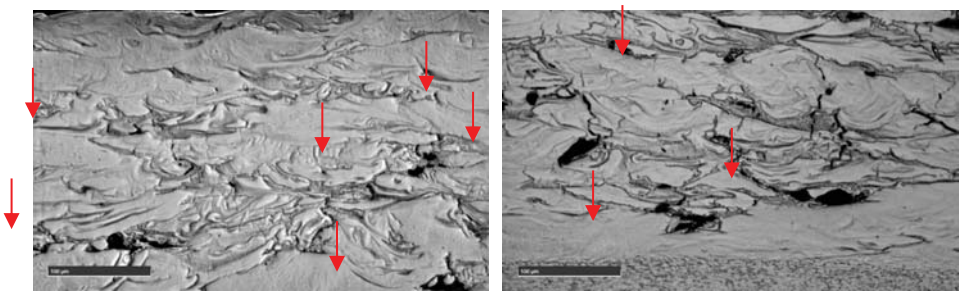

(a) (b)

Fig. 8. Cross-sections of 10 layer samples at 170 W, 1.4 m/s (a) and 340 W and 2.4 m/s (b), balling effect. Black colour is porosity.

At laser power 170 W and scanning speed 0.8-1.0 m/s and 340 W and scanning speed of 1.2 m/s, and hatch distance of 80 μm non-porous 10 layer samples were formed (Fig. 9).

Distribution of elements in the 10-layer samples were not always perfectly homogeneous (Fig. 10). According to SEM EDS, a gradient zone, where the substrate contributed in the chemical composition of the coatings started at 200-250 μm in depth. Point chemical analysis showed that variations of Cu are present within the layer. For example, areas with about 25 wt.%Cu and 15 wt.%Cu were observed in specimen manufactured at 170 W 1.0 m/s, and 340 W 2.0 m/s respectively.

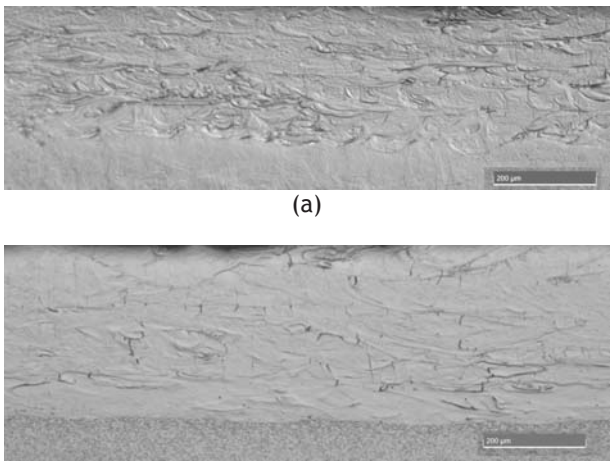

(a)

(b)

Fig. 9. Cross-sections of 10-layer samples (etched by Kroll's reagent) at 170 W and 0.8 m/s (a) and 340 W and 1.2 m/s (b). Images by optical microscope.

The most homogeneous were specimens manufactured at 170W and 0.4 m/s and 340 W and 0.8 m/s. Nevertheless, those specimens contained porosity and were manufactured in a keyhole regime. Higher energy input has positive effect on the homogeneity of the elements; this could be ascribed to fluid flow caused by higher temperate gradients and the re-melting of previous layers due to the large penetration depth (approximately 4 times powder layer thickness see Fig. 5).

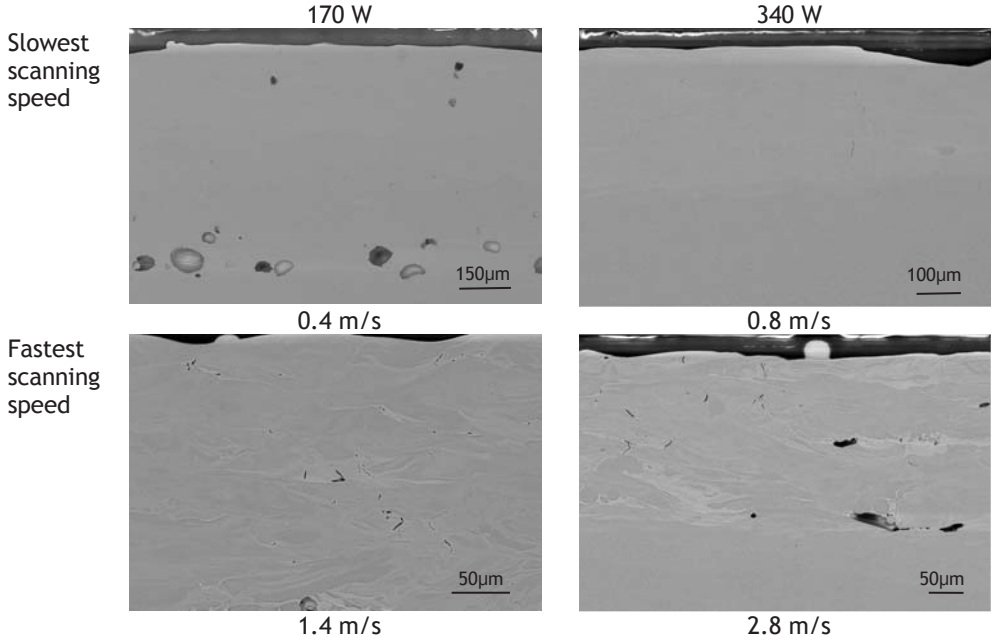

Fig. 10. Comparison between maximum and minimum energy input at the different laser powers. BSE SEM images.

No unmolten Cu particles were observed in any specimens. Some round particles observed on etched cross sections were, according to the EDS observations unmolten particles of Ti6Al4V alloy as shown in Figure 11.

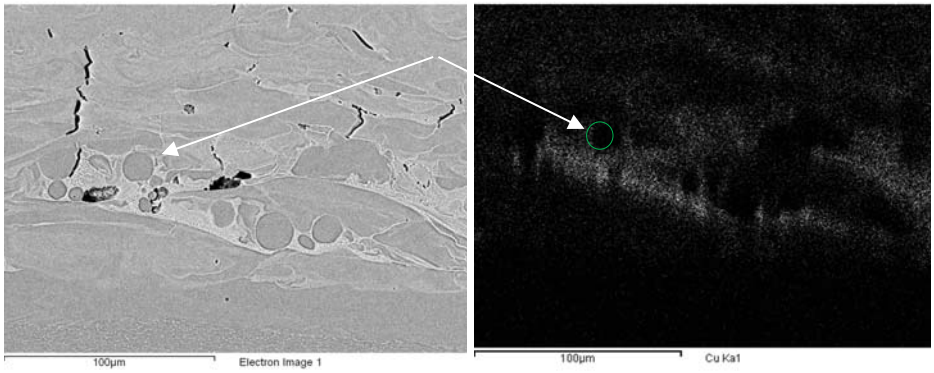

Fig. 11. EDS observations of unmolten Ti6Al4V alloy particles at 340 W and 2.8 m/s (indicated by arrows). Scanning electron image (a) and inhomogeneous copper distribution in white (b).

Possibly due to volatilization, concentration of Cu compared to the nominal values of the feedstock, the specimens were slightly lower than nominal 5 at%Cu in powder mixture.

All recorded data is presented in Table. 1. Non-porous and homogenous samples can be produced at 170 W, between 0.6 and 1.0 m/s and 340 W near 1.2 m/s.

Table 1: Summary of findings for all parameters.

170 W		340 W	
0.4 m/s	Big pores, elements homogeneous	0.8 m/s	Small porosity, elements homogeneous
0.6 m/s	Small porosity, elements homogeneous	1.2 m/s	Non-porous, elements homogeneous
0.8 m/s	Non-porous, elements slightly inhomogeneous	1.6 m/s	Small pores, elements inhomogeneous
1.0 m/s	Non-porous, elements slightly inhomogeneous	2.0 m/s	Pores, elements inhomogeneous
1.2 m/s	Unmolten Ti6Al4V, pores, elements inhomogeneous	2.4 m/s	Unmolten Ti6Al4V, pores, elements inhomogeneous
1.4 m/s	Unmolten Ti6Al4V, pores, elements inhomogeneous	2.8 m/s	Unmolten Ti6Al4V, pores, elements inhomogeneous

3. CONCLUSION

The purpose of this paper was to identify optimal process parameters for in-situ alloying of Ti6Al4V-5 at.%Cu. Better homogeneity is achieved at higher energy input. Further work that could be carried out includes investigation of the distribution of the elements at higher layer thickness with similar parameters, and further fine tuning of optimal parameters. This paper showed that the process window is very small and homogeneity of copper within this zone needs further refinement. Antimicrobial activity, mechanical properties and microstructure of in-situ alloyed Ti6Al4V-5at.% Cu needs further investigation.

REFERENCES

[1] Goldfarb, C. *et al.,* 2017. Ambulatory surgical centers: A Review of complications and adverse events, *Journal of the American Academy of Orthopaedic Surgeons*, 25(1), pp 12-22.

[2] Song Z., *et al.,* 2013. Prosthesis Infections after Orthopedic Joint Replacement: The Possible Role of Bacterial Biofilms. *Orthop Rev (Pavia).* 7 5(2), pp. e14.

[3] Gepreel, A.-H. & Niinomi, M., 2013 Biocompatibility of Ti-alloys for long-term implantation. *J. Mech. Behav. Biomed. Mater.* 20, pp. 407-415.

[4] Li, M., *et al.*, 2016. Towards a molecular understanding of the antibacterial mechanism of Copper-bearing Titanium alloys against Staphylococcus aureus. *Adv. Healthc. Mater.* 5(5), pp. 557–566.

[5] Liu, J., *et al.,* 2014. Effect of Cu content on the antibacterial activity of titanium–copper sintered alloys. *Mater. Sci. Eng. C.* 35, pp. 392–400.

[6] DebRoy *et al.,* 2018, Additive manufacturing of metallic components – Process, structure and properties, *Progress in Materials Science*, 92, pp. 112-224.

[7] du Plessis, A., *et. al.,* 2018. X-ray micro computed tomography in additive manufacturing: a review of the current technology and applications. *3D printing and Additive Manufacturing*, 5 (3), https://doi.org/10.1089/3dp.2018.0060

[8] Yadroitsev, I., *et al.,* 2007. Parametric analysis of the selective laser melting process. *Appl. Surf. Sci.* 253 (19), pp. 8064-8069.

[9] Khairallah, S.A. et al., 2016. Laser powder-bed fusion additive manufacturing: Physics of complex melt flow and formation mechanisms of pores, spatter, and denudation zones. *Acta Materialia*, 108, pp. 36-45.

[10] King, W.E. *et al.,* 2014. Observation of keyhole-mode laser melting in laser powder-bed fusion additive manufacturing. *Journal of Materials Processing Technology*, 214 (12), pp. 2915-2925.

[11] Courtois, M. *et al.,* 2014. A complete model of keyhole and melt pool dynamics to analyze instabilities and collapse during laser welding. *Journal of Laser Applications.* 26 (4), pp. 04200-9.

[12] Yadroitsava I.*et al.,* 2015. Peculiarities of single track formation from TI6AL4V alloy at different laser power densities by SLM. *The South African Journal of Industrial Engineering*, 26 (3), pp. 86-95.

[13] Yadroitsev, I. *Selective Laser Melting: Direct Manufacturing of 3D-Objects by Selective Laser Melting of Metal Powders*; Lambert Academic Publishing: Saarbrücken, Germany, 2009.

[14] Tucho, M., *et al.,* 2018. Investigation of effects of process parameters on microstructure and hardness of SLM manufactured SS316L. *Journal of Alloys and Compounds*, 740, 910-925.